

DSC-Ritz method for high-mode frequency analysis of thick shallow shells

C. W. Lim^{1,*}, Z. R. Li¹ and G. W. Wei²

¹*Department of Building and Construction, City University of Hong Kong, Tat Chee Avenue, Kowloon, Hong Kong*

²*Department of Mathematics and Department of Electrical and Computer Engineering, Michigan State University, East Lansing, MI 48824, U.S.A.*

SUMMARY

This paper addresses a challenging problem in computational mechanics—the analysis of thick shallow shells vibrating at high modes. Existing methods encounter significant difficulties for such a problem due to numerical instability. A new numerical approach, DSC-Ritz method, is developed by taking the advantages of both the discrete singular convolution (DSC) wavelet kernels of the Dirichlet type and the Ritz method for the numerical solution of thick shells with all possible combinations of commonly occurred boundary conditions. As wavelets are localized in both frequency and co-ordinate domains, they give rise to numerical schemes with optimal accurate, stability and flexibility. Numerical examples are considered for Mindlin plates and shells with various edge supports. Benchmark solutions are obtained and analyzed in detail. Experimental results validate the convergence, stability, accuracy and reliability of the proposed approach. In particular, with a reasonable number of grid points, the new DSC-Ritz method is capable of producing highly accurate numerical results for high-mode vibration frequencies, which are hitherto unavailable to engineers. Moreover, the capability of predicting high modes endows us the privilege to reveal a discrepancy between natural higher-order vibration modes of a Mindlin plate and those calculated via an analytical relationship linking Kirchhoff and Mindlin plates. Copyright © 2004 John Wiley & Sons, Ltd.

KEY WORDS: discrete singular convolution; thick shell; high mode; wavelet; vibration frequency; eigenvalue; shear deformable

1. INTRODUCTION

For decades, the vibration analysis of shell structures has been an important research topic due to their wide applications in structural, aerospace and mechanical engineering. One of

*Correspondence to: C. W. Lim, Department of Building and Construction, City University of Hong Kong, Tat Chee Avenue, Kowloon, Hong Kong, People's Republic of China.

†E-mail: bccwlim@cityu.edu.hk

Contract/grant sponsor: City University of Hong Kong

Contract/grant sponsor: Michigan State University

Received 18 February 2004

Revised 7 May 2004

Accepted 29 June 2004

the most successful theories for plates and shells is based on the Kirchhoff–Love hypothesis [1–4], which assumes that the thickness of the plate is very small comparing to its shortest dimension. However, as the shell thickness increases, the classical Kirchhoff–Love theory loses its validity because of the transverse shear strain. To accommodate this effect the Reissner–Mindlin plate theory [5, 6], commonly used in thick plate analysis [5–9], has been extended to shell studies [4, 10, 11], which yields linearly varying transverse shear strain in contrast to the constant distribution. A shear correction factor is therefore introduced to compensate for the errors resulting from the approximation of non-linear transverse shear strain distribution by the linear distribution. Since then, extensive research work has been conducted in the field.

Analytical solution to Reissner–Mindlin plates and shells is certainly valuable for basic understanding of dynamics of plate and shell structures. Unfortunately, exact solutions are scarce and limited to structures of simple geometries and support conditions, such as plates with two opposite edges simply supported [1, 2, 7, 9–12]. As a consequence, numerical solutions of Reissner–Mindlin plates and shells are indispensable for engineering prediction and design. There has been much achievement in computational methodology for shell analysis in the past two decades. Significant approaches include, but are not limited to, finite element [13], finite strip [14], and differential quadrature [15]. Based on the Ritz extremum energy approach, a numerical procedure with geometrically compliant shape functions has been developed by Lim and his associates to solve the vibratory characteristics of thin [16, 17] and thick shallow shells [18–21] subject to a variety of boundary constraints. Using this approach, shape functions are formed from the product of two-dimensional polynomials and appropriate basic functions which ensure the satisfaction of piecewise boundary geometric conditions. This method avoids the difficulty of global methods for implementing boundary conditions. However, there are still a few challenging problems in the analysis of plates and shells, and more precisely in computational mechanics in general, that call for new computational methods, as point out by Zienkiewicz [22]. One example of this class of problems is the prediction and optimal control of deformation, fatigue and fracture of thin-walled structures, such as plates and shells, under high frequency vibrations [22, 23]. In spite of much effort, the numerical prediction of high frequency vibrations in man-made structures remains a challenging task due to the numerical instability of existing computational methods. Low order methods, like h -version finite element methods, converge slowly for higher-order modes [22, 23]. Standard global methods fail to work for higher-order modes due to numerical round-off errors when the degree of polynomial is increased to a certain level. Nevertheless, a complete understanding of a number of very important engineering systems relies on accurate predictive capabilities of high-frequency response. For instance, such understanding is of crucial importance in aerospace structures, e.g. aircraft, rotocrafts, satellites and other space vehicles. Typically, these man-made structures are constantly subjected to various forms of high frequency excitation, which may arise from either mechanical or acoustical sources, such as jet noise, propeller noise, rotor noise, and combustion turbulence from an engine. Structural response to external excitation can lead to either on-resonance (i.e. forced vibration) or fast energy dissipation (i.e. heat production). Excessive vibration and unacceptable noise can create great fluctuations of mechanical loads and stresses, and lead to fatigue failure of structural components, loosening of threaded connection, friction and wear, and damage of electronic and other delicate components. There is a pressing need for the prediction and control of the high frequency vibration and noise levels at the structural design stage and this in turn requires the availability of analysis methods that are able to predict the structural response, as argued by Langley and Bardell [23]. This is the

focus of this work, where we propose to develop a new computational scheme for the analysis and design of plate and shell structures whose performance is governed by high frequency vibrations.

Recently, the discrete singular convolution (DSC) algorithm [24–34] has emerged as a novel approach for the computer realization of singular integrations. The mathematical foundation of the DSC algorithm is the theory of distributions and wavelet analysis. Mathematically, wavelets are functions generated from a single function by two classes of operations, dilation and translation. Wavelets form building blocks for some space, such as a Hilbert space, whether as a frame or as an orthonormal basis. Such building blocks are computationally important when they have certain regularity and localization in both the time and frequency domains. The time-frequency location of wavelets results in *controllable* accuracy for numerical discretization and achieves near optimal computational efficiency. Sequence of approximation to the singular kernels of Hilbert, Abel and delta types are constructed using wavelets [24]. These transforms have important applications to analytical signal processing, tomography and surface interpolation. Numerical solutions to differential equations are formulated via the singular kernels of delta type. By appropriately selecting parameters in the DSC kernel, the DSC approach exhibits controllable accuracy for integration and shows excellent flexibility in handling complex geometries and boundary conditions. It was demonstrated [25] that different implementations of the DSC algorithm, such as global, local, Galerkin, collocation, and finite difference, etc., can be deduced from a single starting point. Thus, the DSC algorithm provides a unified representation to these numerical methods. Many DSC kernels, such as the (regularized) Shannon delta sequence kernel, the (regularized) Dirichlet delta sequence kernel, the (regularized) Lagrange delta sequence kernel and the (regularized) de la Vallée Poussin delta sequence kernel, have been constructed [24].

More recently, the DSC algorithm has found its success in fluid dynamic simulation [27, 28] and electromagnetic wave propagation [29]. More recently the DSC has also been introduced to solve problems in structural mechanics [27, 30] for beams [31] and plates [32–34]. In particular, it has been showed that extremely high frequency vibration modes can be predicted very accurately by using the DSC for plates with simply supported and clamped edges [34]. However, as the governing differential equation is discretized using a collocation approach in these analyses [30–34], further study is required for the collocation approach to be applicable to problems involving free edge supports.

Most recently, a DSC-Ritz method has been proposed to extend the DSC algorithm for treatment of free edge supports in Mindlin plates [35]. In the new method, advantages are taken from both localized DSC kernels and geometrically compliant Ritz basic functions. As a consequence, the DSC-Ritz method exhibits excellent flexibility for handling the free boundary conditions. The DSC kernels used in the previous DSC-Ritz method are the so-called DSC kernels of the positive type, which theoretically can lead to better approximations for non-smooth functions that satisfy the Lipschitz condition. However, it turns out that DSC kernels of the positive type converge less rapidly for problems involving high frequency oscillations. Therefore, it is expensive to use the previous DSC-Ritz for the prediction of high order vibration modes in structural analysis.

In light of the various problems outlined above, this work intends to develop a new DSC-Ritz method which make use of DSC kernels of the Dirichlet type and the Ritz basic boundary functions to arrive at a new approach which is not only able to accommodate a variety of combinations of boundary conditions but also able to obtain accurate numerical solutions for

high-mode vibration frequency parameters. Moreover, the present work introduces the DSC algorithm for the vibration analysis of shells with a variety of possible boundary conditions. Extensive numerical experiments are conducted to validate the convergence and test the accuracy of the proposed method. Experimental results indicate that the new DSC-Ritz method provide accurate prediction of thousands of vibration modes, which, in shell analysis, have been hitherto unavailable to engineers.

With the new capability of predicting high-frequency parameters, the new DSC-Ritz gives us the privilege to reveal an important limitation of a formal analytical relationship [12, 36–39] which converts frequency parameters of a Kirchhoff plate into those of a Mindlin plate. The present finding indicates that a family of shear deformable vibration modes in the Mindlin plate could be missing if the prediction is solely based on the relationship with the vibration modes computed from the Kirchhoff plate.

It is to point out that albeit the proposed DSC-Ritz method has a distinct mathematical foundation, it shares some common features with a class of meshless methods, such as the smooth particle hydrodynamics [40, 41], reproducing kernel particle method [42], radial basis functions [43], and element-free kp-Ritz method [44]. The latter makes use of the cubic spline function to construct the shape function and the penalty method to enforce essential boundary conditions. This similarity enhances our understanding of the philosophy of both the previous meshless type of methods and the present DSC-Ritz scheme.

2. THEORETICAL AND NUMERICAL FORMULATION

2.1. Discrete singular convolution

Singular convolutions (SC) are a special class of mathematical transformations appearing in many problems in science and engineering such as Hilbert transform, Abel transform and Radon transform [24]. It is most convenient to discuss singular convolutions in the context of the theory of distributions [45], which has a significant impact in mathematical analysis and physical sciences. It provides a rigorous justification for a number of informal manipulations in engineering and has significant influence over many mathematical disciplines, such as operator calculus, differential equations, functional analysis, harmonic analysis, and wavelet theory.

Let T denote a singular kernel and $\eta(x)$ be an element of the space of test functions. A singular convolution is defined as

$$F(t) = (T^* \eta)(t) = \int_{-\infty}^{+\infty} T(t-x)\eta(x) dx \quad (1)$$

Depending on the form of the kernel T , the singular convolution is the key issue for a wide range of problems in science and engineering, e.g. Hilbert transform, Abel transform, Radon transform, etc. In the context of this paper, we consider the singular kernels of the delta type

$$T(x) = \delta^{(n)}(x), \quad (n = 0, 1, 2, \dots) \quad (2)$$

Here, kernel $T(x) = \delta(x)$ is the delta distribution and is of particular importance for interpolation of curves and surfaces. Higher order kernels such as $T(x) = \delta^{(n)}(x)$ for $(n = 1, 2, \dots)$ are essential for numerical analysis of differential equations, image processing, noise estimation,

etc. However these kernels cannot be directly applied in computers because they are tempered distributions and do not have a value anywhere. Hence, the singular convolution in Equation (1) is of little direct numerical merit. To avoid the difficulty of using singular expressions directly in computer, we need to construct sequences of approximations (T_α) to the distribution T

$$\lim_{\alpha \rightarrow \alpha_0} T_\alpha(x) \rightarrow T(x) \quad (3)$$

where α_0 is a generalized limit. Obviously, in the case of $T(x) = \delta(x)$, each element in the sequence, $T_\alpha(x)$, is a delta sequence kernel. With a sufficiently smooth approximation, it is useful to consider a discrete singular convolution

$$F_\alpha(t) = \sum_k T_\alpha(t - x_k) f(x_k) \quad (4)$$

where $F_\alpha(t)$ is the approximation of $F(t)$ and $\{x_k\}$ is an appropriate set of discrete points on which the DSC in Equation (4) is well defined. Note that, the original test function $\eta(x)$ is replaced by $f(x)$.

Obviously, as the Fourier transform of the delta distribution is unit in the Fourier domain, the distribution can be regarded as a *universal reproducing kernel* [24]

$$f(x) = \int \delta(x - x') f(x') dx' \quad (5)$$

As a consequence, delta sequence kernels are approximate reproducing kernels or bandlimited reproducing kernels that provide good approximation to the universal reproducing kernel in certain frequency bands.

There are many delta sequence kernels arising in the theory of partial differential equations, Fourier transforms, signal processing and wavelet analysis, with completely different mathematical properties. The reader is referred to References [24, 32] for an elaboration on historical aspects of the delta distribution and its approximations. For the purpose of numerical computations, the delta sequence kernels of both (i) positive type and (ii) Dirichlet type are of particular importance and they have very distinct mathematical and numerical properties.

Let $\{\delta_\alpha\}$ be a sequence of kernel functions on $(-\infty, \infty)$ which are integrable over every bounded interval. We define $\{\delta_\alpha\}$ a delta sequence kernel of Dirichlet type if

1. $\int_{-a}^a \delta_\alpha \rightarrow 1$ as $\alpha \rightarrow \alpha_0$ for some finite constant a .
2. For every constant $\gamma > 0$, $(\int_{-\infty}^{-\gamma} + \int_{\gamma}^{\infty}) \delta_\alpha \rightarrow 0$ as $\alpha \rightarrow \alpha_0$.
3. There are positive constants C_1 and C_2 such that $|\delta_\alpha(x)| \leq C_1/|x| + C_2$ for all x and a .

Although the delta sequence kernels of the Dirichlet type have been extensively studied [24, 25] in context of collocation formulation, their use in the Ritz variation principle has not been explored yet. The object of the present work is to develop a new DSC-Ritz method that utilizes the DSC kernels of the Dirichlet type. For simplicity, we focus on two typical kernels of the Dirichlet type, Shannon's delta sequence kernel

$$\delta_\alpha(x) = \frac{\sin(\alpha x)}{\pi x} \quad (6)$$

and a simplified de la Vallée Poussin delta kernel

$$\delta_\alpha(x) = \frac{1}{\pi\alpha} \frac{\cos(\alpha x) - \cos(2\alpha x)}{x^2} \quad (7)$$

to realize the proposed DSC-Ritz method. Shannon's delta sequence kernel is a wavelet scaling function and has been wide used in wavelet theory and signal processing. It is also known as the sinc function in numerical analysis. However, since it decays slowly asymptotically, it incurs too much error to be used in practical computations.

According to the theory of distributions, the smoothness, regularity and localization of a tempered distribution can be improved by a function of the Schwartz class [45]. It is suggested in Reference [46] that a *delta regularizer* $R_\sigma(x)$ is used in regularizing a delta kernel. A good example is the Gaussian

$$R_\sigma(x) = e^{-x^2/2\sigma^2} \quad (8)$$

Therefore, Shannon's delta sequence kernel in Equation (6) and de la Vallée Poussin delta kernel in Equation (7) can be modified in their regularized form as

$$\delta_{\sigma,\alpha}(x) = \frac{\sin(\alpha x)}{\pi x} e^{-x^2/2\sigma^2} \quad (9)$$

and

$$\delta_{\sigma,\alpha}(x) = \frac{1}{\pi\alpha} \frac{\cos(\alpha x) - \cos(2\alpha x)}{x^2} e^{-x^2/2\sigma^2} \quad (10)$$

These regularized kernels converge extremely fast for approximating functions and their derivatives, and thus can be truncated for a finite domain, which is required in computations. These expressions are chosen to construct new Ritz shape functions. However, many other DSC kernels [24, 26, 32] can be similarly used.

2.2. Problem definition and governing eigenvalue equation

Consider a homogeneous, isotropic, thick doubly curved shallow shell of rectangular planform with length a , width b and thickness h as shown in Figure 1. The principal radii of curvature at the mid-surface ($z = 0$) are denoted by R_x and R_y and the curvature ratio R_y/R_x determines whether the shell has negative (hyperbolic paraboloidal), zero (cylindrical) or positive (spherical) Gaussian curvature. The deflections are resolved into three orthogonal components in the x -, y - and z -directions. The edge surfaces of the shell are either free (denoted by F), soft- or hard-simply supported (S) [20] or clamped (C).

In this paper, we assume first-order shear deformable orthogonal deflection components u , v , and w in terms of their mid-surface orthogonal displacements u_0 , v_0 , w_0 and rotations θ_1^u and θ_1^v as follows:

$$u = \left(1 + \frac{z}{R_x}\right) u_0 + z\theta_1^u \quad (11a)$$

$$v = \left(1 + \frac{z}{R_y}\right) v_0 + z\theta_1^v \quad (11b)$$

$$w = w_0 \quad (11c)$$

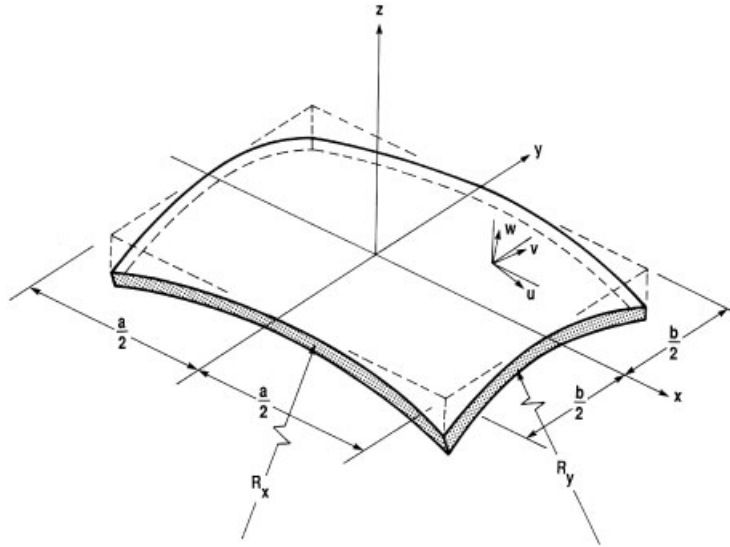


Figure 1. A doubly curved shallow shell with positive Gaussian curvature $1/R_x R_y > 0$.

Further, assuming transverse inextensibility $\varepsilon_z = 0$, the normal and shear strain fields can be expressed as

$$\varepsilon_x = \frac{1}{1 + z/R_x} \left(\frac{\partial u}{\partial x} + \frac{w}{R_x} \right) \quad (12a)$$

$$\varepsilon_y = \frac{1}{1 + z/R_y} \left(\frac{\partial u}{\partial y} + \frac{w}{R_y} \right) \quad (12b)$$

$$\varepsilon_z = 0 \quad (12c)$$

$$\gamma_{yz} = \frac{1}{1 + z/R_y} \left(\frac{\partial w}{\partial y} - \frac{v}{R_y} \right) + \frac{\partial v}{\partial z} \quad (12d)$$

$$\gamma_{xz} = \frac{1}{1 + z/R_x} \left(\frac{\partial w}{\partial x} - \frac{u}{R_x} \right) + \frac{\partial v}{\partial z} \quad (12e)$$

and

$$\gamma_{xy} = \frac{1}{1 + z/R_y} \frac{\partial u}{\partial y} + \frac{1}{1 + z/R_x} \frac{\partial v}{\partial x} \quad (12f)$$

Substituting Equations (11a)–(11c) into Equations (12a)–(12f) results in a strain field in terms of the orthogonal displacements and rotations at the mid-surface

$$\varepsilon_x = \frac{\partial u_0}{\partial x} + \frac{w_0}{R_x} + z \frac{\partial \theta_1^u}{\partial x} - \frac{z^2}{R_x} \frac{\partial \theta_1^u}{\partial x} \quad (13a)$$

$$\varepsilon_y = \frac{\partial v_0}{\partial y} + \frac{w_0}{R_y} + z \frac{\partial \theta_1^v}{\partial y} - \frac{z^2}{R_y} \frac{\partial \theta_1^v}{\partial y} \quad (13b)$$

$$\varepsilon_z = 0 \quad (13c)$$

$$\gamma_{yz} = \frac{\partial w_0}{\partial y} + \theta_1^v - \frac{z}{R_y} \left(\frac{\partial w_0}{\partial y} + \theta_1^v \right) \quad (13d)$$

$$\gamma_{xz} = \frac{\partial w_0}{\partial x} + \theta_1^u - \frac{z}{R_x} \left(\frac{\partial w_0}{\partial x} + \theta_1^u \right) \quad (13e)$$

$$\begin{aligned} \gamma_{xy} = & \frac{\partial u_0}{\partial y} + \frac{\partial v_0}{\partial x} + z \left[\left(\frac{1}{R_y} - \frac{1}{R_x} \right) \left(\frac{\partial v_0}{\partial x} - \frac{\partial u_0}{\partial y} \right) + \frac{\partial \theta_1^u}{\partial y} + \frac{\partial \theta_1^v}{\partial x} \right] \\ & - z^2 \left(\frac{1}{R_y} \frac{\partial \theta_1^u}{\partial y} + \frac{1}{R_x} \frac{\partial \theta_1^v}{\partial x} \right) \end{aligned} \quad (13f)$$

The strain and kinetic energy components of a thick shallow shell are, respectively

$$U = \frac{E}{2(1-\mu^2)} \iiint_V \left[\varepsilon_x^2 + 2\mu\varepsilon_x\varepsilon_y + \frac{1-\mu}{2} (\kappa^2\gamma_{yz}^2 + \kappa^2\gamma_{xz}^2 + \gamma_{xy}^2) \right] dV \quad (14)$$

and

$$T = \frac{\rho}{2} \iiint_V \left[\left(\frac{\partial u}{\partial t} \right)^2 + \left(\frac{\partial v}{\partial t} \right)^2 + \left(\frac{\partial w}{\partial t} \right)^2 \right] dV \quad (15)$$

where E is the Young's modulus, μ is the Poisson ratio, κ^2 is the shear correction factor [5, 6], V is the volume and ρ is the mass density per unit volume. No normal stress is assumed in the above expressions.

Further more, assuming small amplitude of free vibration, the displacement and rotation fields can be approximated by sinusoidal functions as

$$(u_0, v_0, w_0, \theta_1^u, \theta_1^v)(x, y, t) = (U_0, V_0, W_0, \Theta_1^u, \Theta_1^v)(x, y) \sin \omega t \quad (16)$$

Substituting Equations (13a)–(13f) and (16) into Equations (14) and (15), the maximum strain and kinetic energy components in a vibratory cycle are

$$\begin{aligned}
 U_{\max} = & \frac{D}{2} \iint_A \left\{ \frac{12}{h^2} \left[\left(\frac{\partial U_0}{\partial x} \right)^2 + \frac{2W_0}{R_x} \frac{\partial U_0}{\partial x} + \left(\frac{W_0}{R_x} \right)^2 \right. \right. \\
 & + \left(\frac{\partial V_0}{\partial y} \right)^2 + \frac{2W_0}{R_y} \frac{\partial V_0}{\partial y} + \left(\frac{W_0}{R_y} \right)^2 \\
 & + 2\mu \left(\frac{\partial U_0}{\partial x} \frac{\partial V_0}{\partial y} + \frac{\partial U_0}{\partial x} \frac{W_0}{R_y} + \frac{\partial V_0}{\partial y} \frac{W_0}{R_x} + \frac{W_0^2}{R_x R_y} \right) \\
 & \left. + \frac{1-\mu}{2} \left(\frac{\partial U_0}{\partial y} \right)^2 + (1-\mu) \frac{\partial U_0}{\partial y} \frac{\partial V_0}{\partial x} + \frac{1-\mu}{2} \left(\frac{\partial V_0}{\partial x} \right)^2 \right] \\
 & + \frac{6\kappa^2(1-\mu)}{h^2} \left[\left(\frac{\partial W_0}{\partial y} \right)^2 + 2 \frac{\partial W_0}{\partial y} \Theta_1^v + (\Theta_1^v)^2 + \left(\frac{\partial W_0}{\partial x} \right)^2 + 2 \frac{\partial W_0}{\partial x} \Theta_1^u + (\Theta_1^u)^2 \right] \\
 & - \frac{2}{R_x} \frac{\partial U_0}{\partial x} \frac{\partial \Theta_1^u}{\partial x} + \left(\frac{\partial \Theta_1^u}{\partial x} \right)^2 - \frac{2}{R_y} \frac{\partial V_0}{\partial y} \frac{\partial \Theta_1^v}{\partial y} + \left(\frac{\partial \Theta_1^v}{\partial y} \right)^2 \\
 & + 2\mu \left(\frac{\partial \Theta_1^u}{\partial x} \frac{\partial \Theta_1^v}{\partial y} - \frac{1}{R_y} \frac{\partial U_0}{\partial x} \frac{\partial \Theta_1^v}{\partial y} - \frac{1}{R_x} \frac{\partial V_0}{\partial y} \frac{\partial \Theta_1^u}{\partial x} \right) \\
 & + \frac{1-\mu}{2} \left[\left(\frac{2}{R_x} - \frac{4}{R_y} \right) \frac{\partial U_0}{\partial y} \frac{\partial \Theta_1^u}{\partial y} + \left(\frac{2}{R_y} - \frac{4}{R_x} \right) \frac{\partial V_0}{\partial x} \frac{\partial \Theta_1^v}{\partial x} - \frac{2}{R_x} \frac{\partial V_0}{\partial x} \frac{\partial \Theta_1^u}{\partial y} \right. \\
 & \left. - \frac{2}{R_y} \frac{\partial U_0}{\partial y} \frac{\partial \Theta_1^v}{\partial x} + \left(\frac{\partial \Theta_1^u}{\partial y} \right)^2 + 2 \frac{\partial \Theta_1^u}{\partial y} \frac{\partial \Theta_1^v}{\partial x} + \left(\frac{\partial \Theta_1^v}{\partial x} \right)^2 \right] \Big\} dx dy \quad (17)
 \end{aligned}$$

and

$$\begin{aligned}
 T_{\max} = & \frac{\rho\omega^2}{2} \iint_A \left\{ h [U_0^2 + V_0^2 + W_0^2] \right. \\
 & \left. + \frac{h^3}{12} \left[\frac{2U_0\Theta_1^u}{R_x} + \left(\frac{U_0}{R_x} \right)^2 + (\Theta_1^u)^2 + \frac{2V_0\Theta_1^v}{R_y} + \left(\frac{V_0}{R_y} \right)^2 + (\Theta_1^v)^2 \right] \right\} dx dy \quad (18)
 \end{aligned}$$

where $D = Eh^3/[12(1-\mu^2)]$ is the flexural rigidity, A is the area of the shell mid-surface, U_{\max} and T_{\max} are maximum strain and maximum kinetic energy components.

A non-dimensional co-ordinate system is introduced as follows

$$\xi = \frac{x}{a} \quad (19a)$$

$$\eta = \frac{y}{b} \quad (19b)$$

$$\varsigma = \frac{z}{h} \quad (19c)$$

Using this non-dimensional co-ordinate system, the displacement and rotation amplitude functions $U_0(\xi, \eta)$, $V_0(\xi, \eta)$, $W_0(\xi, \eta)$, $\Theta_1^u(\xi, \eta)$ and $\Theta_1^v(\xi, \eta)$ given in Equation (16) can be repressed by

$$U_0(\xi, \eta) = \sum_{i=1}^m c_i^u \phi_i^u(\xi, \eta) \quad (20a)$$

$$V_0(\xi, \eta) = \sum_{i=1}^m c_i^v \phi_i^v(\xi, \eta) \quad (20b)$$

$$W_0(\xi, \eta) = \sum_{i=1}^m c_i^w \phi_i^w(\xi, \eta) \quad (20c)$$

$$\Theta_1^u(\xi, \eta) = \sum_{i=1}^m \bar{c}_i^u \Phi_i^u(\xi, \eta) \quad (20d)$$

$$\Theta_1^v(\xi, \eta) = \sum_{i=1}^m \bar{c}_i^v \Phi_i^v(\xi, \eta) \quad (20e)$$

in which c_i^u , c_i^v , c_i^w , \bar{c}_i^u , \bar{c}_i^v are the unknown coefficients and ϕ_i^u , ϕ_i^v , ϕ_i^w , Φ_i^u , Φ_i^v are the corresponding shape functions.

Based on the principle of extremum energy, an energy functional defined as

$$\Pi = U_{\max} - T_{\max} \quad (21)$$

is minimized with respect to the unknown coefficients

$$\frac{\partial \Pi}{\partial c_i^u} = 0 \quad (22a)$$

$$\frac{\partial \Pi}{\partial c_i^v} = 0 \quad (22b)$$

$$\frac{\partial \Pi}{\partial c_i^w} = 0 \quad (22c)$$

$$\frac{\partial \Pi}{\partial \bar{c}_i^u} = 0 \quad (22d)$$

$$\frac{\partial \Pi}{\partial \bar{c}_i^v} = 0 \quad (22e)$$

where

$$\begin{aligned} \frac{\partial U_{\max}}{\partial c_i^u} = \frac{D}{ab} \sum_{j=1}^m & \left[\frac{12b^2}{h^2} c_j^u I_{\phi_i^u \phi_j^u}^{1010} + \frac{6a^2(1-\mu)}{h^2} c_j^u I_{\phi_i^u \phi_j^u}^{0101} + \frac{12ab\mu}{h^2} c_j^v I_{\phi_i^u \phi_j^v}^{1001} \right. \\ & + \frac{6ab(1-\mu)}{h^2} c_j^v I_{\phi_i^u \phi_j^v}^{0110} + \frac{12ab^2}{h^2} \left(\frac{1}{R_x} + \frac{\mu}{R_y} \right) c_j^w I_{\phi_i^u \phi_j^w}^{1000} - \frac{b^2}{R_x} \bar{c}_j^u I_{\phi_i^u \Phi_j^u}^{1010} \\ & \left. + \frac{a^2(1-\mu)}{2} \left(\frac{1}{R_x} - \frac{2}{R_y} \right) \bar{c}_j^u I_{\phi_i^u \Phi_j^u}^{0101} - \frac{ab\mu}{R_y} \bar{c}_j^v I_{\phi_i^u \Phi_j^v}^{1001} - \frac{ab(1-\mu)}{2R_y} \bar{c}_j^v I_{\phi_i^u \Phi_j^v}^{0110} \right] \quad (23a) \end{aligned}$$

$$\begin{aligned} \frac{\partial U_{\max}}{\partial c_i^v} = \frac{D}{ab} \sum_{j=1}^m & \left[\frac{12ab\mu}{h^2} c_j^u I_{\phi_i^v \phi_j^u}^{0110} + \frac{6ab(1-\mu)}{h^2} c_j^u I_{\phi_i^v \phi_j^u}^{1001} + \frac{12a^2}{h^2} c_j^v I_{\phi_i^v \phi_j^v}^{0101} \right. \\ & + \frac{6b^2(1-\mu)}{h^2} c_j^v I_{\phi_i^v \phi_j^v}^{1010} + \frac{12a^2b}{h^2} \left(\frac{\mu}{R_x} + \frac{1}{R_y} \right) c_j^w I_{\phi_i^v \phi_j^w}^{0100} - \frac{ab\mu}{R_x} \bar{c}_j^u I_{\phi_i^v \Phi_j^u}^{0110} \\ & \left. + \frac{ab(1-\mu)}{2R_x} \bar{c}_j^u I_{\phi_i^v \Phi_j^u}^{1001} - \frac{a^2}{R_y} \bar{c}_j^v I_{\phi_i^v \Phi_j^v}^{0101} + \frac{b^2(1-\mu)}{2} \left(\frac{1}{R_y} - \frac{2}{R_x} \right) \bar{c}_j^v I_{\phi_i^v \Phi_j^v}^{1010} \right] \quad (23b) \end{aligned}$$

$$\begin{aligned} \frac{\partial U_{\max}}{\partial c_i^w} = \frac{D}{ab} \sum_{j=1}^m & \left[\frac{12ab^2}{h^2} \left(\frac{1}{R_x} + \frac{\mu}{R_y} \right) c_j^u I_{\phi_i^w \phi_j^u}^{0010} + \frac{12a^2b}{h^2} \left(\frac{\mu}{R_x} + \frac{1}{R_y} \right) c_j^v I_{\phi_i^w \phi_j^v}^{0001} \right. \\ & + \frac{12a^2b^2}{h^2} \left(\frac{1}{R_x^2} + \frac{2\mu}{R_x R_y} + \frac{1}{R_y^2} \right) c_j^w I_{\phi_i^w \phi_j^w}^{0000} + \frac{6a^2\kappa^2(1-\mu)}{h^2} c_j^w I_{\phi_i^w \phi_j^w}^{0101} \\ & + \frac{6b^2\kappa^2(1-\mu)}{h^2} c_j^w I_{\phi_i^w \phi_j^w}^{1010} + \frac{6ab^2\kappa^2(1-\mu)}{h^2} \bar{c}_j^u I_{\phi_i^w \Phi_j^u}^{1000} \\ & \left. + \frac{6a^2b\kappa^2(1-\mu)}{h^2} \bar{c}_j^v I_{\phi_i^w \Phi_j^v}^{0100} \right] \quad (23c) \end{aligned}$$

$$\begin{aligned} \frac{\partial U_{\max}}{\partial \bar{c}_i^u} = & \frac{D}{ab} \sum_{j=1}^m \left[\frac{a^2(1-\mu)}{2} \left(\frac{1}{R_x} - \frac{2}{R_y} \right) c_j^u I_{\Phi_i^u \Phi_j^u}^{0101} - \frac{b^2}{R_x} c_j^u I_{\Phi_i^u \Phi_j^u}^{1010} - \frac{ab\mu}{R_x} c_j^v I_{\Phi_i^u \Phi_j^v}^{1001} \right. \\ & - \frac{ab(1-\mu)}{2R_x} c_j^v I_{\Phi_i^u \Phi_j^v}^{0110} + \frac{6ab^2\kappa^2(1-\mu)}{h^2} c_j^w I_{\Phi_i^u \Phi_j^w}^{0010} + \frac{6a^2b^2\kappa(1-\mu)}{h^2} \bar{c}_j^u I_{\Phi_i^u \Phi_j^u}^{0000} \\ & \left. + b^2 \bar{c}_j^u I_{\Phi_i^u \Phi_j^u}^{1010} + \frac{a^2(1-\mu)}{2} \bar{c}_j^u I_{\Phi_i^u \Phi_j^u}^{0101} + ab\mu \bar{c}_j^v I_{\Phi_i^u \Phi_j^v}^{1001} + \frac{ab(1-\mu)}{2} \bar{c}_j^v I_{\Phi_i^u \Phi_j^v}^{0110} \right] \quad (23d) \end{aligned}$$

$$\begin{aligned} \frac{\partial U_{\max}}{\partial \bar{c}_i^v} = & \frac{D}{ab} \sum_{j=1}^m \left[-\frac{ab\mu}{R_y} c_j^u I_{\Phi_i^v \Phi_j^u}^{0110} - \frac{ab(1-\mu)}{2R_y} c_j^u I_{\Phi_i^v \Phi_j^u}^{1001} - \frac{a^2}{R_y} c_j^v I_{\Phi_i^v \Phi_j^v}^{1001} \right. \\ & - \frac{b^2(1-\mu)}{2} \left(\frac{1}{R_y} - \frac{2}{R_x} \right) c_j^v I_{\Phi_i^v \Phi_j^v}^{1010} + \frac{6a^2b\kappa^2(1-\mu)}{h^2} c_j^w I_{\Phi_i^v \Phi_j^w}^{0001} + ab\mu \bar{c}_j^u I_{\Phi_i^v \Phi_j^u}^{0110} \\ & + \frac{ab(1-\mu)}{2} \bar{c}_j^u I_{\Phi_i^v \Phi_j^u}^{1001} + \frac{6a^2b^2\kappa(1-\mu)}{h^2} \bar{c}_j^v I_{\Phi_i^v \Phi_j^v}^{0000} \\ & \left. + a^2 \bar{c}_j^v I_{\Phi_i^v \Phi_j^v}^{0101} + \frac{b^2(1-\mu)}{2} \bar{c}_j^v I_{\Phi_i^v \Phi_j^v}^{1010} \right] \quad (23e) \end{aligned}$$

$$\frac{\partial T_{\max}}{\partial c_i^u} = \rho h \omega^2 ab \sum_{j=1}^m \left[\left(1 + \frac{h^2}{12R_x^2} \right) c_j^u I_{\Phi_i^u \Phi_j^u}^{0000} + \frac{h^2}{12R_x} \bar{c}_j^u I_{\Phi_i^u \Phi_j^u}^{0000} \right] \quad (24a)$$

$$\frac{\partial T_{\max}}{\partial c_i^v} = \rho h \omega^2 ab \sum_{j=1}^m \left[\left(1 + \frac{h^2}{12R_y^2} \right) c_j^v I_{\Phi_i^v \Phi_j^v}^{0000} + \frac{h^2}{12R_x} \bar{c}_j^v I_{\Phi_i^v \Phi_j^v}^{0000} \right] \quad (24b)$$

$$\frac{\partial T_{\max}}{\partial c_i^w} = \rho h \omega^2 ab \sum_{j=1}^m \bar{c}_j^u I_{\Phi_i^w \Phi_j^w}^{0000} \quad (24c)$$

$$\frac{\partial T_{\max}}{\partial \bar{c}_i^u} = \rho h \omega^2 ab \sum_{j=1}^m \left[\frac{h^2}{12R_x} c_j^u I_{\Phi_i^u \Phi_j^u}^{0000} + \frac{h^2}{12} \bar{c}_j^u I_{\Phi_i^u \Phi_j^u}^{0000} \right] \quad (24d)$$

$$\frac{\partial T_{\max}}{\partial \bar{c}_i^v} = \rho h \omega^2 ab \sum_{j=1}^m \left[\frac{h^2}{12R_y} c_j^v I_{\Phi_i^v \Phi_j^v}^{0000} + \frac{h^2}{12} \bar{c}_j^v I_{\Phi_i^v \Phi_j^v}^{0000} \right] \quad (24e)$$

Substituting Equations (23a)–(23e) and (24a)–(24e) into Equations (22a)–(22e) yields a governing eigenvalue equation as follows

$$(\mathbf{K} - \lambda^2 \mathbf{M})\{\mathbf{C}\} = \{0\} \quad (25)$$

The stiffness matrix \mathbf{K} , mass matrix \mathbf{M} and the coefficient vector \mathbf{C} are

$$\mathbf{K} = \begin{bmatrix} k^{uu} & k^{uv} & k^{uw} & k^{u\theta_u} & k^{u\theta_v} \\ & k^{vv} & k^{vw} & k^{v\theta_u} & k^{v\theta_v} \\ & & k^{ww} & k^{w\theta_u} & k^{w\theta_v} \\ & & & k^{\theta_u\theta_u} & k^{\theta_u\theta_v} \\ \text{sym} & & & & k^{\theta_v\theta_v} \end{bmatrix} \quad (26a)$$

$$\mathbf{M} = \begin{bmatrix} m^{uu} & [0] & [0] & m^{u\theta_u} & [0] \\ & m^{vv} & [0] & [0] & m^{v\theta_v} \\ & & m^{ww} & [0] & [0] \\ & & & m^{\theta_u\theta_u} & [0] \\ \text{sym} & & & & m^{\theta_v\theta_v} \end{bmatrix} \quad (26b)$$

and

$$\mathbf{C} = \{ \{c^u\} \{c^v\} \{c^w\} a\{\bar{c}^u\} b\{\bar{c}^v\} \}^T \quad (26c)$$

As noted in Equations (20a)–(20e), the dimensions of c_i^u , c_i^v , c_i^w and \bar{c}_i^u , \bar{c}_i^v are different. To ensure the same dimensions in the coefficient vector in Equation (26c), $a\{\bar{c}^u\}$ and $b\{\bar{c}^v\}$ are chosen instead of $\{\bar{c}^u\}$ and $\{\bar{c}^v\}$ which will improve the condition number of the stiffness matrix \mathbf{K} and mass matrix \mathbf{M} . The elements of the stiffness and mass matrices are

$$k_{ij}^{uu} = \frac{12b^2}{h^2} I_{\phi_i^u \phi_j^u}^{1010} + \frac{6a^2(1-\mu)}{h^2} I_{\phi_i^u \phi_j^u}^{0101} \quad (27a)$$

$$k_{ij}^{uv} = \frac{12ab\mu}{h^2} I_{\phi_i^u \phi_j^v}^{1001} + \frac{6ab(1-\mu)}{h^2} I_{\phi_i^u \phi_j^v}^{0110} \quad (27b)$$

$$k_{ij}^{uw} = \frac{12ab^2}{h^2} \left(\frac{1}{R_x} + \frac{\mu}{R_y} \right) I_{\phi_i^u \phi_j^w}^{1000} \quad (27c)$$

$$k_{ij}^{u\theta_u} = -\frac{b^2}{aR_x} I_{\phi_i^u \phi_j^u}^{1010} + \frac{a(1-\mu)}{2} \left(\frac{1}{R_x} - \frac{2}{R_y} \right) I_{\phi_i^u \phi_j^u}^{0101} \quad (27d)$$

$$k_{ij}^{u\theta_v} = -\frac{a\mu}{R_y} I_{\phi_i^u \phi_j^v}^{1001} - \frac{a(1-\mu)}{2R_y} I_{\phi_i^u \phi_j^v}^{0110} \quad (27e)$$

$$k_{ij}^{vv} = \frac{12a^2}{h^2} I_{\phi_i^v \phi_j^v}^{0101} + \frac{6b^2(1-\mu)}{h^2} I_{\phi_i^v \phi_j^v}^{1010} \quad (27f)$$

$$k_{ij}^{vw} = \frac{12ab^2}{h^2} \left(\frac{\mu}{R_x} + \frac{1}{R_y} \right) I_{\phi_i^v \phi_j^w}^{0100} \quad (27g)$$

$$k_{ij}^{v\theta_u} = -\frac{b\mu}{R_x} I_{\phi_i^v \Phi_j^u}^{0110} - \frac{b(1-\mu)}{2R_x} I_{\phi_i^v \Phi_j^u}^{1001} \quad (27h)$$

$$k_{ij}^{v\theta_v} = \frac{b(1-\mu)}{2} \left(\frac{1}{R_y} - \frac{2}{R_x} \right) I_{\phi_i^v \Phi_j^v}^{1010} - \frac{a^2}{bR_y} I_{\phi_i^v \Phi_j^v}^{0101} \quad (27i)$$

$$k_{ij}^{ww} = \frac{12a^2b^2}{h^2} \left(\frac{1}{R_x^2} + \frac{2\mu}{R_x R_y} + \frac{1}{R_y^2} \right) I_{\phi_i^w \phi_j^w}^{0000} \\ + \frac{6a^2\kappa^2(1-\mu)}{h^2} I_{\phi_i^w \phi_j^w}^{0101} + \frac{6b^2\kappa^2(1-\mu)}{h^2} I_{\phi_i^w \phi_j^w}^{1010} \quad (27j)$$

$$k_{ij}^{w\theta_u} = \frac{6b^2\kappa^2(1-\mu)}{h^2} I_{\phi_i^w \Phi_j^u}^{1000} \quad (27k)$$

$$k_{ij}^{w\theta_v} = \frac{6a^2\kappa^2(1-\mu)}{h^2} I_{\phi_i^w \Phi_j^v}^{0100} \quad (27l)$$

$$k_{ij}^{\theta_u\theta_u} = \frac{6b^2\kappa^2(1-\mu)}{h^2} I_{\Phi_j^u \Phi_j^u}^{0000} + \frac{b^2}{a^2} I_{\Phi_j^u \Phi_j^u}^{1010} + \frac{(1-\mu)}{2} I_{\Phi_j^u \Phi_j^u}^{0101} \quad (27m)$$

$$k_{ij}^{\theta_u\theta_v} = I_{\Phi_j^u \Phi_j^v}^{1001} + \frac{(1-\mu)}{2} I_{\Phi_j^u \Phi_j^v}^{0110} \quad (27n)$$

$$k_{ij}^{\theta_v\theta_v} = \frac{6a^2\kappa^2(1-\mu)}{h^2} I_{\Phi_j^v \Phi_j^v}^{0000} + \frac{a^2}{b^2} I_{\Phi_j^v \Phi_j^v}^{0101} + \frac{(1-\mu)}{2} I_{\Phi_j^v \Phi_j^v}^{1010} \quad (27o)$$

and

$$m_{ij}^{uu} = \left(1 + \frac{h^2}{12R_x^2} \right) I_{\phi_i^u \phi_j^u}^{0000} \quad (28a)$$

$$m_{ij}^{u\theta_u} = \frac{h^2}{12aR_x} I_{\phi_i^u \Phi_j^u}^{0000} \quad (28b)$$

$$m_{ij}^{vv} = \left(1 + \frac{h^2}{12R_y^2} \right) I_{\phi_i^v \phi_j^v}^{0000} \quad (28c)$$

$$m_{ij}^{v\theta_v} = \frac{h^2}{12bR_y} I_{\phi_i^v \Phi_j^v}^{0000} \quad (28d)$$

$$m_{ij}^{ww} = I_{\phi_i^w \phi_j^w}^{0000}; \quad m_{ij}^{\theta_u \theta_u} = \frac{h^2}{12a^2} I_{\Phi_i^u \Phi_j^u}^{0000}; \quad m_{ij}^{\theta_v \theta_v} = \frac{h^2}{12b^2} I_{\Phi_j^v \Phi_i^v}^{0000} \tag{28e-f}$$

in which

$$I_{\phi_i^\alpha \phi_j^\beta}^{defg} = \iint_A \frac{\partial^{d+e} \phi_i^\alpha(\zeta, \eta)}{\partial \zeta^d \partial \eta^e} \frac{\partial^{f+g} \phi_j^\beta(\zeta, \eta)}{\partial \zeta^d \partial \eta^e} d\zeta d\eta \tag{29}$$

where $\phi, \vartheta = \phi, \Phi$; $\alpha, \beta = u, v, w$; $i, j = 1, 2, \dots, m$ and m is the total number of terms employed in the shape functions.

The eigenvalue or equivalently the non-dimensional frequency parameter of the governing eigenvalue equation (25) is

$$\lambda = \frac{b\sqrt{12(1-\mu^2)}}{h} \lambda' \tag{30a}$$

where

$$\lambda' = \omega a \sqrt{\frac{\rho}{E}} \tag{30b}$$

The above formulation can be reduced to those of a flat plate if the radii of curvature are infinite which is equivalent to unity of the Lamé parameters.

2.3. The DSC-Ritz method

In this study, a new set of shape functions needs to be employed which is able to approximate the deflection of the whole domain and at the same time satisfies the prescribed boundary conditions. These shape functions are formed from the product of sets of two-dimensional localized DSC kernels and basic functions which associate the piecewise boundary geometric expressions. The new shape functions φ_k^α ($\varphi = \phi, \Phi$ and $\alpha = u, v, w$) can be expressed as

$$\varphi_k^\alpha(\zeta, \eta) = f_k(\zeta, \eta) \varphi_b^\alpha \tag{31}$$

where φ_b^α is the basic function. The two-dimensional DSC kernel $\sum_{k=1}^m f_k(\zeta, \eta)$ are given by

$$\sum_{k=1}^m f_k(\zeta, \eta) = \sum_{i=1}^n \sum_{j=1}^n \delta_{\sigma ij}(\zeta, \eta) \tag{32}$$

where n is the number of grid points adopted in both ζ -direction and η -direction, and

$$m = n^2, \quad k = (i - 1) \times n + j \tag{33}$$

Note that $\delta_{\sigma ij}$ in Equation (32) is a DSC delta kernel and the two-dimensional forms for the aforementioned two DSC kernels in Equations (9)–(10) can be constructed by tensor products as

$$\delta_{\sigma ij}(\zeta, \eta) = \frac{\sin[(\pi/\Delta)(\zeta - \xi_i)] \sin[(\pi/\Delta)(\eta - \eta_j)]}{(\pi^2/\Delta^2)(\zeta - \xi_i)(\eta - \eta_j)} e^{-[(\zeta - \xi_i)^2/2\sigma^2]} e^{-[(\eta - \eta_j)^2/2\sigma^2]} \tag{34}$$

for Shannon's kernel, and

$$\begin{aligned} \delta_{\sigma ij}(\xi, \eta) = & \frac{\cos[(\pi/\bar{\Delta})(\xi - \xi_i)] - \cos[(2\pi/\bar{\Delta})(\xi - \xi_i)]}{[(\pi/\bar{\Delta})(\xi - \xi_i)]^2} e^{-[(\xi - \xi_i)^2/2\sigma^2]} \\ & \times \frac{\cos[(\pi/\bar{\Delta})(\eta - \eta_j)] - \cos[(2\pi/\bar{\Delta})(\eta - \eta_j)]}{[(\pi/\bar{\Delta})(\eta - \eta_j)]^2} e^{-[(\eta - \eta_j)^2/2\sigma^2]} \end{aligned} \quad (35)$$

for de la Vallée Poussin kernel. In all the above kernels, ξ_i and η_j are grid point along the ξ -axis and η -axis, respectively. The parameters σ and $\bar{\Delta}$ are chosen as $\sigma = r\Delta$; $\bar{\Delta} = \frac{3}{2}\Delta$, where Δ is the grid spacing, and r is an adjustable parameter determining the radius of influence. Noted that r is dependent on the kernels and it is also slightly influenced by the grid number. In general, a larger r leads to a better result but too large r will result in the collapse of computation. In the present paper, it is chosen from 2.0 to 2.5.

The basic function φ_b^α ($\varphi = \phi, \Phi$ and $\alpha = u, v, w$) is a set of kinematically oriented geometric functions. They are defined by the products of the equations of continuous piecewise boundary geometries of the shell planform each raised to an appropriate power depending on the type of boundary constraints imposed on the shell. For a thick shallow shell, the basic functions for the SSSS shell are

$$\phi_b^u = (\xi^2 - 0.25)(\eta^2 - 0.25) \quad (36a)$$

$$\phi_b^v = (\xi^2 - 0.25)(\eta^2 - 0.25) \quad (36b)$$

$$\phi_b^w = (\xi^2 - 0.25)(\eta^2 - 0.25) \quad (36c)$$

$$\Phi_b^u = (\eta^2 - 0.25) \quad (36d)$$

$$\Phi_b^v = (\xi^2 - 0.25) \quad (36e)$$

and the CCCC shell are

$$\phi_b^u = (\xi^2 - 0.25)(\eta^2 - 0.25) \quad (37a)$$

$$\phi_b^v = (\xi^2 - 0.25)(\eta^2 - 0.25) \quad (37b)$$

$$\phi_b^w = (\xi^2 - 0.25)(\eta^2 - 0.25) \quad (37c)$$

$$\Phi_b^u = (\xi^2 - 0.25)(\eta^2 - 0.25) \quad (37d)$$

$$\Phi_b^v = (\xi^2 - 0.25)(\eta^2 - 0.25) \quad (37e)$$

Although only two types of boundary conditions are presented for brevity, more detailed basic functions for a variety of boundary constraints are available in References [20, 21].

An efficient computer programme of the DSC-Ritz method has been developed in Fortran. It is based on the p -Ritz method [36] developed previous by one of the authors. However, the p -shape functions are replaced by DSC kernel shape functions here. The Gaussian numerical integration method is employed here for domain integration. To ensure the accuracy of the numerical results, a fine Gaussian integration scheme is necessary. In addition, the numerical procedure is far more efficient than a FE analysis of a similar structure in terms of computational time and numerical accuracy.

3. NUMERICAL EXAMPLES AND DISCUSSION

In this section, we consider numerical consistency, stability and accuracy of the DSC-Ritz method through convergence and comparison studies. Throughout the numerical examples, the Poisson ratio μ and shear correction factor κ^2 are chosen as 0.3 and 5/6, respectively.

3.1. Convergence studies

Tables I and II present the convergence study of two typical examples of shells with SSSS and CCCC boundary conditions of square planform ($a/b = 1$) and shallowness ratio ($b/R_y = 0.5$). The curvature ratio (R_y/R_x) investigated is 1 while the thickness ratios are 0.1 and 0.2. The convergence patterns of the first eight non-dimensional frequency parameters $\lambda' = \omega a \sqrt{\rho/E}$ have been investigated by varying the number of uniform DSC grid points n from 2 to 10 in both ξ - and η -directions. The results are summarized in Tables I and II with the influence parameter $r = 2.3$ for the Shannon kernel and $r = 2.5$ for the de la Vallée Poussin kernel, respectively. The numerical results are compared with those of the p -Ritz method [20].

In Tables I and II, it is obviously that λ' decreases as the number of DSC grid points increases from 2 to 10. For most cases in Table I, the frequency parameters for the SSSS plate have achieved good convergence when the number of grid points $n \geq 6$. When the number of grid points n increases from 6 to 9, λ' is very close to the results in Reference [20]. The same convergence trend is observed in Table II for the CCCC shell. The result differs a little from that in Reference [20] as different basic functions for boundary constraints are adopted. Also it can be found that both Shannon's kernel and de la Vallée Poussin's kernel are able to yield frequency parameters as accurate and reliable as required with a reasonable number of grid points.

3.2. Comparison of results

The accuracy and efficiency of the DSC-Ritz method is to be further established through a comparison of frequency parameters $\lambda = \omega a^2 \sqrt{\rho h/D} / \pi^2$ with those from other computational methods and exact solutions, especially in the high frequency domain. First we present the convergence study of a square ($a/b = 1$) Mindlin plate with SSSS boundary conditions and thickness ratio $h/a = 0.1$. For frequencies of rectangular Kirchhoff plates with SSSS boundary conditions, an explicit analytical solution is available. The corresponding frequency for a Mindlin plate can be deduced via a formal relationship between a Kirchhoff plate and

Table I. Convergence of $\lambda' = \omega a \sqrt{\rho/E}$ for a SSSS thick doubly-curved shallow shell with $\nu = 0.3$, $a/b = 1.0$, $b/R_y = 0.5$ and $R_y/R_x = 1$.

h/b	Kernel	n	Mode sequence number							
			1	2	3	4	5	6	7	8
0.1	Shannon	2	0.96572	3.5197	3.5197	3.9712	3.9712	4.6532	5.1016	5.7658
		4	0.94336	1.5355	1.5355	2.2600	2.9955	3.0057	3.5789	3.5789
		6	0.94322	1.4808	1.4808	2.1876	2.6256	2.6347	3.2736	3.2736
		8	0.94312	1.4805	1.4805	2.1873	2.6251	2.6342	3.2731	3.2731
		10	0.94307	1.4806	1.4806	2.1874	2.6250	2.6341	3.2731	3.2731
	de la Poussin Vallée [20]	2	0.96590	3.5214	3.5214	3.9722	3.9722	4.6565	5.1032	5.7655
		4	0.94326	1.5385	1.5385	2.2641	3.0027	3.0130	3.5861	3.5861
		6	0.94312	1.4809	1.4809	2.1877	2.6255	2.6346	3.2736	3.2736
		8	0.94305	1.4804	1.4804	2.1873	2.6250	2.6341	3.2730	3.2730
		10	0.94300	1.4805	1.4805	2.1873	2.6249	2.6340	3.2730	3.2730
0.2	Shannon	2	1.3236	3.5439	3.5439	3.9857	3.9857	4.6506	5.1019	5.7616
		4	1.2904	2.4325	2.4325	3.4581	3.7582	3.7582	4.3483	4.3587
		6	1.2904	2.3637	2.3637	3.3851	3.7544	3.7544	3.9765	3.9844
		8	1.2904	2.3633	2.3633	3.3847	3.7540	3.7540	3.9759	3.9838
		10	1.2904	2.3634	2.3634	3.3848	3.7539	3.7539	3.9758	3.9837
	de la Vallée Poussin [20]	2	1.3243	3.5456	3.5456	3.9868	3.9868	4.6540	5.1035	5.7614
		4	1.2903	2.4363	2.4363	3.4622	3.7583	3.7583	4.3570	4.3674
		6	1.2903	2.3638	2.3638	3.3852	3.7543	3.7543	3.9765	3.9843
		8	1.2903	2.3632	2.3632	3.3847	3.7540	3.7540	3.9758	3.9837
		10	1.2903	2.3633	2.3633	3.3848	3.7539	3.7539	3.9757	3.9836
	[20]	—	1.2900	2.3631	2.3631	3.3846	3.7537	3.7537	3.9755	3.9835

a Mindlin plate as [12, 36–39]

$$\omega_i^2 = \frac{6\kappa^2 G}{\rho h^2} \left\{ \left[1 + \frac{1}{12} \widehat{\omega}_i h^2 \sqrt{\frac{\rho h}{D}} \Upsilon \right] - \sqrt{\left[1 + \frac{1}{12} \widehat{\omega}_i h^2 \sqrt{\frac{\rho h}{D}} \Upsilon^2 \right] - \frac{\rho h^2}{3\kappa^2 G} \widehat{\omega}_i^2} \right\} \tag{38}$$

$$\Upsilon = 1 + \frac{2}{\kappa^2(1 - \mu)}$$

where $i = 1, 2, \dots$, corresponds to the mode sequence number and ω_i and $\widehat{\omega}_i$ correspond to the frequency of a Kirchhoff plate and a Mindlin plate, respectively. From Equation (38), accurate frequency for simply supported Mindlin plate can be derived from the known Kirchhoff plate vibration solutions. However, as pointed out by Mindlin *et al.* [7], three independent families of modes are possible when the Mindlin plate edges are simply supported. It is found that the vibration modes corresponding to that of Kirchhoff plate are just a subset of the spectrum of Mindlin plate. Therefore, it should be mentioned that the Mindlin plate frequencies deduced from Equation (38) are valid only when the two kinds of plates have the same vibration mode shape. Here, we compute the first 1500 mode frequencies by Shannon’s kernel

Table II. Convergence of $\lambda' = \omega a \sqrt{\rho/E}$ for a CCCC thick doubly-curved shallow shell with $\nu = 0.3$, $a/b = 1.0$, $b/R_y = 0.5$ and $R_y/R_x = 1$.

h/b	Kernel	n	Mode sequence number								
			1	2	3	4	5	6	7	8	
0.1	Shannon	2	1.6850	3.4137	3.4137	3.9060	3.9060	4.6531	4.6954	5.7176	
		4	1.2166	1.9515	1.9515	2.6941	3.7437	3.7437	3.7979	3.8760	
		6	1.2118	1.9466	1.9466	2.6894	3.1459	3.1900	3.7144	3.7144	
		8	1.2107	1.9452	1.9452	2.6873	3.1414	3.1861	3.7127	3.7127	
		10	1.2104	1.9447	1.9447	2.6866	3.1398	3.1847	3.7122	3.7122	
	de la Vallée Poussin	2	1.6901	3.4168	3.4168	3.9077	3.9077	4.6565	4.6985	5.7174	
		4	1.2164	1.9514	1.9514	2.6937	3.7439	3.7439	3.8118	3.8901	
		6	1.2117	1.9464	1.9464	2.6892	3.1456	3.1897	3.7143	3.7143	
		8	1.2106	1.9451	1.9451	2.6872	3.1412	3.1860	3.7127	3.7127	
		10	1.2103	1.9446	1.9446	2.6865	3.1398	3.1846	3.7121	3.7121	
	[20]	—	1.2106	1.9447	1.9447	2.6888	3.1471	3.1915	3.7149	3.7149	
	0.2	Shannon	2	1.9763	3.4870	3.4870	3.9206	3.9206	4.6500	4.7372	5.7005
			4	1.7647	2.8292	2.8292	3.7671	3.7671	3.8014	4.4363	4.5555
			6	1.7618	2.8276	2.8276	3.7657	3.7657	3.7999	4.3139	4.3883
8			1.7613	2.8271	2.8271	3.7655	3.7655	3.7992	4.3127	4.3872	
10			1.7611	2.8268	2.8268	3.7655	3.7655	3.7990	4.3125	4.3870	
de la Vallée Poussin		2	1.9797	3.4897	3.4897	3.9223	3.9223	4.6534	4.7401	5.7002	
		4	1.7646	2.8291	2.8291	3.7672	3.7672	3.8012	4.4363	4.5640	
		6	1.7618	2.8275	2.8275	3.7657	3.7657	3.7997	4.3139	4.3883	
		8	1.7612	2.8270	2.8270	3.7655	3.7655	3.7992	4.3127	4.3872	
		10	1.7611	2.8268	2.8268	3.7654	3.7654	3.7990	4.3125	4.3870	
[20]		—	1.7638	2.8281	2.8281	3.7653	3.7653	3.8062	4.3337	4.4078	

and de la Vallée Poussin's kernel. In order to ensure the accuracy of the results, the number of DSC grid points is set to 32 with parameter $r = 2.22$ for the Shannon kernel and $r = 2.38$ for the de la Vallée Poussin kernel. In Table III, the results from this analysis up to as high as the 1500-mode are listed together with the frequencies computed from Equation (38). It can be seen that the numerical results accord with the ones deduced from Equation (38) very well for modes below 112. For these modes, the Mindlin plate has similar corresponding vibration modes as Kirchhoff plate. Beyond mode-112, the mode sequence number begins to mismatch due to the presence of shear deformable modes which the Kirchhoff-Mindlin relationship fails to predict. It indicates that the Mindlin plate has more complicated vibration modes than those of the Kirchhoff plate in high frequency domain and Equation (38) should be used with care. The last mode-1500 in Table III is not present in the Kirchhoff plate analysis and thus it is a shear deformable mode.

Another comparison of the present results with exact solutions and finite element solutions is also carried out for a doubly curved thin cap with square planform and free boundary conditions. The latter means that both the in-plane deflection components tangential to an edge (u along the edges $\eta = -0.5, 0.5$ and v along the edges $\zeta = -0.5, 0.5$) and the transverse deflection component (w) are constrained. While the in-plane deflection components normal to

Table III. Comparison of frequency parameter $\lambda = \omega a^2 \sqrt{\rho h / D} / \pi^2$ for a SSSS thick square Mindlin plate with $\nu = 0.3$ and $h/a = 0.1$. Values in parenthesis indicate the mode sequence number corresponding to Kirchhoff–Mindlin relationship [36].

Mode sequence number	Frequency from Kirchhoff–Mindlin relationship [36]	Shannon	de la Vallée Poussin
1	1.9317	1.9362	1.9360
⋮	⋮	⋮	⋮
10	13.539	13.541	13.541
⋮	⋮	⋮	⋮
20	22.351	22.354	22.353
⋮	⋮	⋮	⋮
30	28.766	28.768	28.768
⋮	⋮	⋮	⋮
40	35.655	35.656	35.656
⋮	⋮	⋮	⋮
50	40.293	40.294	40.294
⋮	⋮	⋮	⋮
60	44.583	44.584	44.584
⋮	⋮	⋮	⋮
70	49.868	49.869	49.869
⋮	⋮	⋮	⋮
80	54.458	54.458	54.458
⋮	⋮	⋮	⋮
90	57.918	57.919	57.919
⋮	⋮	⋮	⋮
100	62.548	62.549	62.549
⋮	⋮	⋮	⋮
112	65.652	65.653	65.652
⋮	⋮	⋮	⋮
152	71.509 (130)	71.510	71.510
⋮	⋮	⋮	⋮
192	76.975 (150)	76.976	76.976
⋮	⋮	⋮	⋮
233	82.944 (170)	82.946	82.946
⋮	⋮	⋮	⋮
277	88.548 (190)	88.549	88.549
⋮	⋮	⋮	⋮
325	94.027 (210)	94.028	94.028
⋮	⋮	⋮	⋮

Table III *Continued.*

Mode sequence number	Frequency from Kirchhoff–Mindlin relationship [36]	Shannon	de la Vallée Poussin
365	98.347 (230)	98.349	98.349
⋮	⋮	⋮	⋮
408	102.84 (250)	102.84	102.84
⋮	⋮	⋮	⋮
513	113.32 (300)	113.32	113.32
⋮	⋮	⋮	⋮
727	132.30 (400)	132.31	132.31
⋮	⋮	⋮	⋮
948	149.18 (500)	149.19	149.19
⋮	⋮	⋮	⋮
1500	—	185.24	185.25

the edges (u along the edges $\xi = -0.5, 0.5$ and v along the edges $\eta = -0.5, 0.5$) are free to move. Employing doubly curved triangular finite elements, Olson and Lindberg [47] solved the spherical cap ($R_y/R_x = 1.0$) problem of square planform ($a/b = 1$) with $R_y h/a^2 = 0.005$. The exact solutions of this shell configuration using the thin shell theory are given by [47]

$$\omega_{mn}^2 = \frac{E}{\rho R^2} \left[1 + \pi^4 \left(\frac{Rh}{a^2} \right)^2 \frac{(m^2 + n^2)^2}{12(1 - \mu^2)} \right] \quad (39)$$

where $R = R_y = R_x$ and m, n are the half-wave numbers in the x and y -directions respectively. In the present work, the first 180 mode frequencies are computed by using Shannon's kernel and de la Vallée Poussin's kernel. A total of 20 DSC grid points is employed with parameter $r = 2.3$ for the Shannon kernel and $r = 2.5$ for the de la Vallée Poussin kernel. The computational results of exact, finite element (only the first 45 mode frequencies are available), and the present DSC solutions are tabulated in Table IV. The non-dimensional frequency parameter is expressed as $\lambda = \rho R^2 \omega^2 / E$. Excellent agreement is achieved between the exact and the present solutions all through. The finite element solutions are satisfactory only for some lower modes.

3.3. Effects of the thickness ratio and curvature ratio on high-mode frequency

A set of numerical studies is carried out for doubly curved shells of square planform ($a/b = 1$) and shallowness ratio $b/R_x = 0.5$ with four different boundary conditions: SSSS, CCCC, SFSF and CFFF. The curvature ratio R_y/R_x ranges from $-2, -1$ (negative Gaussian curvature corresponding to a hyperbolic paraboloidal shell) to $1, 2$ (positive Gaussian curvature corresponding to a spherical shell). The thickness ratio ranges from 0.02 (a thin shell) to 0.2 (a thick shell). The first 500 mode frequencies are presented. In the calculation, de la Vallée Poussin

Table IV. Comparison of frequency parameter $\lambda = \rho R^2 \omega^2 / E$ for the freely doubly-curved cap having square planform with $\nu = 0.3$, $R_y/R_x = 1.0$ and $Rh/a^2 = 0.005$.

Mode sequence number	Exact solution [47]	Finite element [47]	Shannon	de la Vallée Poussin
1	1.00089	1.00092	0.99931	0.99963
⋮	⋮	⋮	⋮	⋮
5	1.02230	1.02297	1.02357	1.02450
⋮	⋮	⋮	⋮	⋮
10	1.06445	1.06679	1.06683	1.06741
⋮	⋮	⋮	⋮	⋮
25	1.22836	1.25510	1.23343	1.23434
⋮	⋮	⋮	⋮	⋮
30	1.45159	1.51743	1.45808	1.45999
⋮	⋮	⋮	⋮	⋮
40	1.82981	1.96834	1.83906	1.84305
⋮	⋮	⋮	⋮	⋮
50	2.18840	—	2.19646	2.19853
⋮	⋮	⋮	⋮	⋮
60	2.61122	—	2.62277	2.62969
⋮	⋮	⋮	⋮	⋮
70	3.27489	—	3.27990	3.27964
⋮	⋮	⋮	⋮	⋮
80	4.00077	—	4.01125	4.01054
⋮	⋮	⋮	⋮	⋮
90	4.65373	—	4.66691	4.67012
⋮	⋮	⋮	⋮	⋮
100	5.68870	—	5.69749	5.68970
⋮	⋮	⋮	⋮	⋮
110	6.22035	—	6.24225	6.22877
⋮	⋮	⋮	⋮	⋮
120	7.44488	—	7.46215	7.45482
⋮	⋮	⋮	⋮	⋮
130	8.30590	—	8.32127	8.33089
⋮	⋮	⋮	⋮	⋮
140	9.65465	—	9.71898	9.69114
⋮	⋮	⋮	⋮	⋮
150	10.3718	—	10.5214	10.4363
⋮	⋮	⋮	⋮	⋮

Table IV *Continued.*

Mode sequence number	Exact solution [47]	Finite element [47]	Shannon	de la Vallée Poussin
160	11.8918	—	12.0940	11.9901
⋮	⋮	⋮	⋮	⋮
170	13.1068	—	13.2207	13.1398
⋮	⋮	⋮	⋮	⋮
180	14.9379	—	15.0098	14.9821

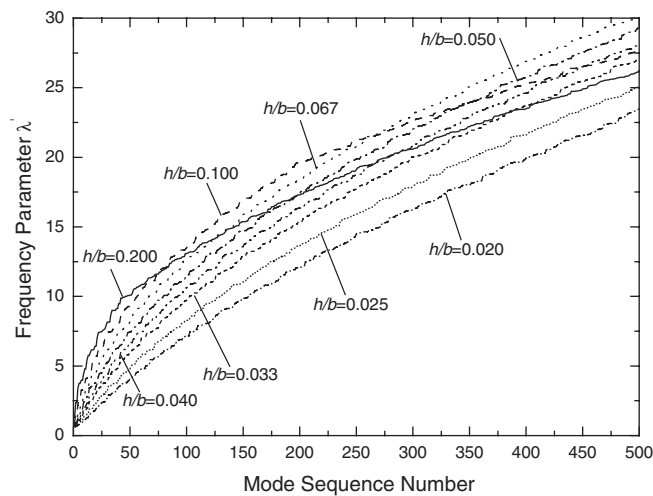


Figure 2. The effect of thickness ratios on the frequency parameter for an SSSS spherical shallow shell with $a/b = 1$, $b/R_x = 0.5$ and $R_y/R_x = 1.0$.

kernel is adopted with the same grid number and parameters used in the computation of the Mindlin plate.

Mode frequencies with different thickness ratios are plotted in Figures 2–5 for four types of boundary conditions, respectively. In Figure 2, it is observed that for a similar mode sequence number, thicker shells demonstrate higher vibration frequencies in the lower-mode region while in higher-mode region thinner shells become stiffer and with higher frequency. For example, the frequency for a thicker shell with $h/b = 0.2$ is higher than that of a thinner shell with $h/b = 0.1$ for modes below approximately 75 in Figure 2. Beyond mode-75, the thicker shell becomes less stiff and the corresponding frequency is lower than that of the thinner shell. Similar facts are also observed in Figures 3–5 for shells with different boundary conditions.

Such phenomenon exhibits due to the effects of shear deformation. In lower-mode region, the effect of shear deformation is less significant and most vibration modes are bending modes. This

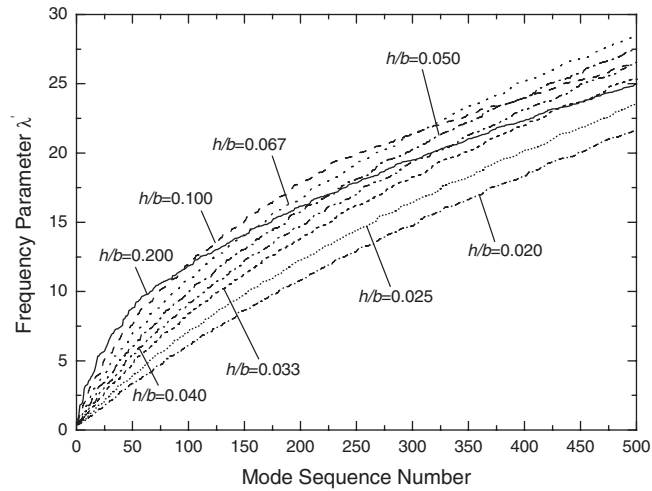


Figure 3. The effect of thickness ratios on the frequency parameter for a CCCC spherical shallow shell with $a/b = 1$, $b/R_x = 0.5$ and $R_y/R_x = 1.0$.

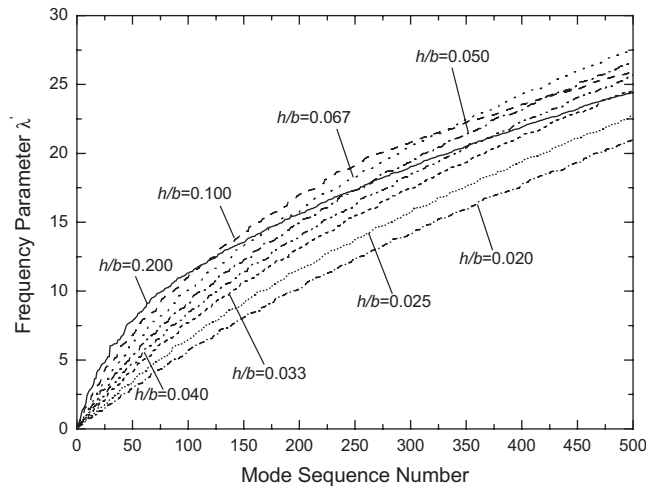


Figure 4. The effect of thickness ratios on the frequency parameter for a CFFF spherical shallow shell with $a/b = 1$, $b/R_x = 0.5$ and $R_y/R_x = 1.0$.

also explains why there is a one-to-one correspondence with identical vibration mode sequence number between the Kirchhoff plate and Mindlin plate via the Kirchhoff–Mindlin relationship [12, 36–39] in the low frequency domain. In higher-mode region, more and more modes occur due to in-plane shear or coupled bending-shear with significant shear effects, which do not exist in the Kirchhoff plate analysis. The Kirchhoff–Mindlin relationship still applies but only for purely bending modes and the mode sequence numbers do not match. Therefore, a lower mode

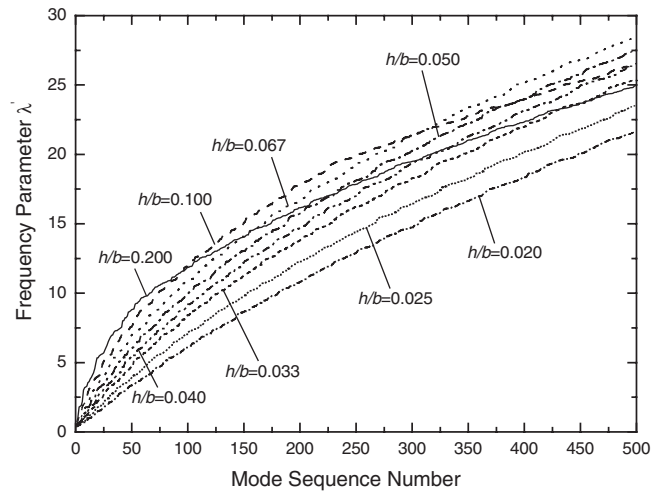


Figure 5. The effect of thickness ratios on the frequency parameter for a SFSF spherical shallow shell with $a/b = 1$, $b/R_x = 0.5$ and $R_y/R_x = 1.0$.

of a Kirchhoff plate can correspond to a higher-mode of a Mindlin plate and the gap is filled with shear-dominant modes. An example is presented in Table III where values in parentheses corresponds to the mode sequence number according to the Kirchhoff plate analysis while, in fact, it corresponds to a higher mode of the Mindlin plate.

The effect of varying the Gaussian curvature is presented in Table V. Obviously, variation in the Gaussian curvature introduces very little effect to the vibration response even in the cases of both negative (hyperbolic paraboloidal) and positive (spherical) Gaussian curvatures. This effect is expected to be more significant when a deep shell is considered which, however, is beyond the scope of the present work.

4. CONCLUSION

Progress has been made in the prediction and analysis of shells vibrating at high frequency modes, which is a severe challenge to existing computational methods due to numerical instability. A new numerical approach, DSC-Ritz method, has been developed in this work to model the vibration of shear deformable doubly-curved rectangular shallow shells. The new numerical scheme is able to yield accurate high-mode frequencies which are hitherto unavailable. The key idea is to combine DSC wavelet kernels of the Dirichlet type and the Ritz basic boundary functions to construct new shape functions. Two typical DSC kernels, regularized Shannon wavelet kernel and regularized de la Vallée Poussin kernel, are introduced to the DSC-Ritz scheme. Energy functionals are expressed in terms of new DSC-Ritz shape functions. The standard Ritz extremum energy principle is employed to determine a set of unknown coefficients via a generalized eigenvalue problem.

Extensive numerical experiments are design to explore the accuracy and test the stability of the proposed method. Convergence and comparison studies are carried out for both Mindlin

Table V. Frequency parameter $\lambda' = \omega a \sqrt{\rho/E}$ for a thick doubly-curved shallow shell with $\nu = 0.3$, $a/b = 1.0$ and $b/R_y = 0.5$.

Boundary condition	R_y/R_x	Mode sequence number							
		1	10	50	100	200	300	400	500
SSSS	-2	0.55064	2.5102	7.5546	11.905	17.864	21.317	23.959	26.475
	-1	0.56587	2.5147	7.5543	11.906	17.864	21.314	23.958	26.471
	1	0.59448	2.5216	7.5723	11.910	17.858	21.328	23.965	26.471
	2	0.56666	2.5137	7.5662	11.904	17.861	21.325	23.963	26.474
CCCC	-2	1.0802	3.7695	9.6106	13.523	19.658	22.948	25.637	28.101
	-1	1.1248	3.7683	9.6136	13.518	19.654	22.948	25.637	28.093
	1	1.2101	3.8162	9.6236	13.542	19.657	22.953	25.644	28.118
	2	1.1256	3.7936	9.6161	13.537	19.659	22.949	25.640	28.114
CFFF	-2	0.19930	1.7711	6.7865	10.994	17.023	20.789	23.561	25.910
	-1	0.21035	1.7775	6.7830	10.996	17.023	20.789	23.557	25.908
	1	0.20568	1.7619	6.7993	10.989	17.020	20.791	23.573	25.901
	2	0.19664	1.7632	6.7944	10.990	17.022	20.790	23.569	25.908
SFSF	-2	0.55064	2.5102	7.5546	11.905	17.864	21.317	23.959	26.475
	-1	0.56587	2.5147	7.5544	11.906	17.864	21.314	23.958	26.471
	1	0.59448	2.5216	7.5723	11.910	17.858	21.328	23.966	26.471
	2	0.56666	2.5138	7.5662	11.904	17.861	21.325	23.962	26.474

plates and thick shells with a variety of boundary conditions. Numerical results indicate that the proposed DSC-Ritz method is very accurate and reliable for the vibration analysis of Mindlin plates and thick shells.

One of the most significant features of the new DSC-Ritz approach is its numerical stability in predicting high frequency vibration modes. Other existing numerical methods fail to provide accurate estimations for high frequency modes of shells due to ill-conditioned matrices or numerical round off errors. The present DSC-Ritz method, aided with DSC wavelet kernels of the Dirichlet type, is able to make accurate predictions for hundreds and thousands of vibration modes. As a by-product, such an unusual ability enables us to discover that the analytical relationship linking Kirchhoff and Mindlin plates does not work for shear deformable vibration modes of the Mindlin plate based on the full set of easy-to-come-by Kirchhoff modes.

ACKNOWLEDGEMENTS

The work described in this paper was supported by a Young/Junior Scholars (YSS) Funding of the City University of Hong Kong.

REFERENCES

1. Timoshenko SP, Woinowsky-Krieger S. *Theory of Plates and Shells* (2nd edn). McGraw-Hill: New York, 1959.
2. Leissa AW. *Vibration of Plates*. NASA SP-160. Scientific and Technical Information Office, NASA: Washington DC, 1969.

3. Leissa AW. *Vibration of Shells*. NASA SP-288. Scientific and Technical Information Office, NASA: Washington DC, 1973.
4. Gould PL. *Analysis of Shells and Plates*. Springer-Verlag: New York, 1988.
5. Reissner E. The effect of transverse shears deformation on the bending of elastic plate. *Journal of Applied Mechanics* 1945; **12**:69–76.
6. Mindlin RD. Influence of rotary inertia and shear in flexural motion of isotropic, elastic plates. *Journal of Applied Mechanics* 1951; **18**:1031–1036.
7. Mindlin RD, Schacknow A, Deresiewicz H. Flexural vibrations of rectangular plates. *Journal of Applied Mechanics* 1956; **71**:430–436.
8. Whitney JM, Sun CT. A higher order theory for extensional motion of laminated composites. *Journal of Sound and Vibration* 1973; **30**:85–97.
9. Bert CW, Chen TLC. Effect of shear deformation on vibration of antisymmetric angle-ply laminated rectangular plates. *International Journal of Solids and Structures* 1978; **14**:465–473.
10. Reddy JN. Exact solutions of moderately thick laminated shells. *Journal of Engineering Mechanics* (ASCE) 1984; **110**:794–809.
11. Reddy JN, Liu CF. A higher-order shear deformation theory of laminated elastic shells. *International Journal of Engineering Science* 1985; **23**:319–330.
12. Wang CM. Natural frequencies formula for simply supported Mindlin plates. *Journal of Vibration and Acoustics* 1994; **116**:536–540.
13. Ozakca M, Hinton E, Rao NVR. Free-vibration analysis and shape optimization of prismatic folded plates and shells with circular curved planform. *International Journal for Numerical Methods in Engineering* 1994; **37**:1713–1739.
14. Cheung YK, Au FTK. Isoparametric spline finite strip for degenerate shells. *Thin-Walled Structures* 1995; **21**:65–92.
15. Redekop D, Xu B. Vibration analysis of toroidal panels using the differential quadrature method. *Thin-Walled Structures* 1999; **34**:217–231.
16. Lim CW, Liew KM. A $pb-2$ Ritz formulation for flexural vibration of shallow cylindrical shells of rectangular planform. *Journal of Sound and Vibration* 1994; **173**:343–375.
17. Lim CW, Kitipornchai S, Liew KM. Modelling the vibration of a variable thickness ellipsoidal dish with central point-clamp or concentric surface-clamp. *The Journal of the Acoustical Society of America* 1996; **99**:362–372.
18. Lim CW, Liew KM. A higher order theory for vibration of shear deformable cylindrical shallow shells. *International Journal of Mechanical Sciences* 1995; **37**:277–295.
19. Lim CW, Liew KM. Vibration of moderately thick cylindrical shallow shells. *The Journal of the Acoustical Society of America* 1996; **100**:3665–3673.
20. Liew KM, Lim CW. A Ritz vibration analysis of doubly-curved rectangular shallow shells using a refined first-order theory. *Computer Methods in Applied Mechanics and Engineering* 1995; **127**:145–162.
21. Liew KM, Lim CW. Vibration studies on moderately thick doubly curved elliptic shallow shells. *Acta Mechanica* 1996; **116**:83–96.
22. Zienkiewicz OC. Achievements and some unsolved problems of the finite element method. *International Journal for Numerical Methods in Engineering* 2000; **47**:9–28.
23. Langley RS, Bardell NS. A review of current analysis capabilities applicable to the high frequency vibration prediction of aerospace structures. *The Aeronautical Journal* 1998; **102**:287–297.
24. Wei GW. Discrete singular convolution for the solution of the Fokker–Planck equations. *Journal of Chemical Physics* 1999; **110**:8930–8942.
25. Wei GW. A unified approach for the solution of the Fokker–Planck equations. *Journal of Physics A* 2000; **33**:4935–4953.
26. Wei GW. Wavelets generated by the discrete singular convolution kernels. *Journal of Physics A* 2000; **33**:8577–8596.
27. Wei GW. A new algorithm for solving some mechanical problems. *Computer Methods in Applied Mechanics and Engineering* 2001; **190**:2017–2030.
28. Zhou YC, Patnaik BSV, Wan DC, Wei GW. DSC solution for flows in a staggered double lid driven cavity. *International Journal for Numerical Methods in Engineering* 2003; **57**:211–234.
29. Bao G, Wei GW, Zhao S. Numerical solution of the Helmholtz equation with high wave numbers. *International Journal for Numerical Methods in Engineering* 2004; **59**:389–408.

30. Wei GW. Vibration analysis by discrete singular convolution. *Journal of Sound and Vibration* 2001; **244**: 535–553.
31. Wei GW. Discrete singular convolution for beam analysis. *Engineering Structure* 2001; **23**:1045–1053.
32. Wei GW, Zhao YB, Xiang Y. Discrete singular convolution and its application to the analysis of plates with internal supports. I Theory and algorithm. *International Journal for Numerical Methods in Engineering* 2002; **55**:913–946.
33. Xiang Y, Zhao YB, Wei GW. Discrete singular convolution and its application to the analysis of plates with internal supports. II Complex supports. *International Journal for Numerical Methods in Engineering* 2002; **55**:947–971.
34. Wei GW, Zhao YB, Xiang Y. A novel approach for the prediction and control of high frequency vibration. *Journal of Sound and Vibration* 2002; **257**:207–246.
35. Hou YS, Wei GW, Xiang Y. DSC-Ritz method for the vibration analysis of Mindlin plates. *International Journal for Numerical Methods in Engineering*, Revised 2003.
36. Liew KM, Wang CM, Xiang Y, Kitipornchai S. *Vibration of Mindlin Plates: Programming the p-Version Ritz Method*. Elsevier: Oxford, 1998.
37. Wang CM, Reddy JN, Lee KH. *Shear Deformable Beams and Plates: Relationships with Classical Solutions*. Elsevier: Singapore, 2000.
38. Wang CM. Vibration frequencies of simply supported polygonal sandwich plates via Kirchhoff solutions. *Journal of Vibration and Vibration* 1996; **190**:255–260.
39. Reddy JN, Wang CM. Relationship between classical and shear deformation theories on axisymmetric circular plates. *AIAA Journal* 1997; **35**:1862–1868.
40. Lucy LB. A numerical approach to the testing of the fission hypothesis. *The Astrophysical Journal* 1977; **82**:1013–1024.
41. Monaghan JJ. An introduction to SPH. *Computer Physics Communication* 1988; **48**:89–96.
42. Liu WK, Jun S, Li S, Adee J, Belytschko T. Reproducing kernel particle method for structural dynamics. *International Journal for Numerical Methods in Engineering* 1995; **38**:1655–1679.
43. Driscoll TA, Fornberg B. Interpolation in the limit of increasingly flat radial basis functions. *Computers and Mathematics with Applications* 2002; **43**:413–422.
44. Zhao X, Liew KM, Ng TN. Vibration analysis of laminated composite cylindrical panels via a meshfree approach. *International Journal of Solids and Structures* 2003; **40**:161–180.
45. Schwartz L. *Théorie des distributions*. Hermann: Paris, 1951.
46. Wei GW, Zhang DS, Kouri DJ, Hoffman DK. Langrange distributed approximating functionals. *Physical Review Letters* 1997; **79**:775–779.
47. Olson MD, Lindberg GM. Dynamic analysis of shallow shell with a double-curved triangular finite element. *Journal of Sound and Vibration* 1971; **19**:299–318.